water

MDPI

Article

Monitoring the Hydrological Balance of a Landslide-Prone Slope Covered by Pyroclastic Deposits over Limestone Fractured Bedrock

Pasquale Marino, Luca Comegna, Emilia Damiano, Lucio Olivares and Roberto Greco *

Dipartimento di Ingegneria, Università degli Studi della Campania "Luigi Vanvitelli", via Roma 9, 81031 Aversa, Italy; pasquale.marino1@unicampania.it (P.M.); luca.comegna@unicampania.it (L.C.); emilia.damiano@unicampania.it (E.D.); lucio.olivares@unicampania.it (L.O.)

* Correspondence: roberto.greco@unicampania.it; Tel.: +39-081-501-0207; Fax: +39-081-503-7370

Received: 7 November 2020; Accepted: 22 November 2020; Published: 25 November 2020

Abstract: Many mountainous areas in Campania, Southern Italy, are characterized by steep slopes covered by loose unsaturated pyroclastic deposits laying upon fractured limestone bedrock. The soil covers are mainly constituted by layers of ashes and pumices. Large and intense rainfall events trigger shallow landslides, often turning into debris flows that cause huge damage and casualties. The slope of Cervinara, around 40 km Northeast of Naples, was involved in a catastrophic flowslide on 16 December 1999, triggered by a rainstorm of 325 mm in 48 h. To capture the main effects of precipitation on the slope stability, hydro-meteorological monitoring activities have been carried out at the slope to assess the water balance for three years (2017–2020). The field monitoring data allowed the identification of the complex hydrological processes involving the unsaturated pyroclastic soil and the shallow groundwater system developing in the limestone bedrock, which control the conditions that potentially predispose the slope to landslide triggering. Specifically, late autumn has been identified as the potentially most critical period, when slope drainage processes are not yet effective, and soil covers already receive large amounts of precipitation.

Keywords: rainfall-induced landslide; shallow landslide; hydrological predisposing cause; field monitoring

1. Introduction

The numerous hydrological processes involving slopes in response to meteorological forces are extremely important to understand the predisposing conditions of rainfall-induced landslide initiation [1–7], neglected or only indirectly considered even in the most recent landslide early warning systems (e.g., [8]). The hydrological predisposing causes are frequently connected with an area exceeding the failed slope, i.e., they are related to large-scale processes (in time and space). The need to assess the water balance, including large-scale hydrological processes, is true for both shallow and deep-seated landslides. On one hand, deep-seated landslides, commonly referred to as deep-seated gravitational slope deformations, are very slow mass movements of a large volume (usually >0.5 km^3) of soil and rock [9–13]. The deformation processes in slopes present various forms [14], and are considered to be precursors of eventual damages [15–17]. Several authors have studied the transition process from gravitational deformation to slide, especially from the mechanical viewpoint [18]. Causal factors include: lithology and geologic structure [19], tectonic and topographic stresses and their concentration [20,21], seismicity [22], changes in groundwater regime [23], and human activity [24]. The hydrogeological response of the groundwater regime for the initiation of deep-seated landslides is strongly correlated with antecedent precipitation history [25,26]. Moreover, the groundwater flow in a

rock landslide, mainly controlled by a very complex fracture network, sometimes plays a key role in the hydrological response of slopes [27–29]. Differently, rainfall-induced shallow landslides usually occur along steep slopes covered with granular deposits, in saturated or unsaturated conditions, following an increase in pore water pressure. The initiation of such landslides mainly depends on the characteristics of the triggering rainfall event, and on the moisture conditions of the soil layer at the beginning of the event [5,30–32]. The triggering factor is preferentially associated with a short period of intense rainfall, while the large-scale hydrological processes occurring in the slope indirectly influence the triggering because they affect the initial conditions (predisposing causes). Hence, to better identify and investigate the complex and different causal preparatory hydrological conditions leading to landslides, a proper large-scale field investigation is often needed.

This paper deals with the hydrological behaviour of slopes covered by layered granular pyroclastic deposits, usually in unsaturated conditions, mainly consisting of ashes and pumices, laying upon fractured limestone bedrock [33], which are typical of many mountainous areas of the Southern Apennines in Campania, Southern Italy. The total thickness of the soil cover is quite variable [34–36]. The equilibrium of such slopes, up to inclination angles of 40–50°, is usually guaranteed by the contribution of soil suction to shear strength [37]. Intense and persistent rainfall events wet the cover, reduce the soil suction, and sometimes lead to shallow landslide triggering, often turning into destructive debris flows that can cause heavy damages and casualties [38]. However, a complete knowledge of the hydrological processes that develop in the soil cover and the possible water exchanges with the underlying bedrock, which may predispose the loose covers to fail, is still lacking. Karst aquifers are often present in fractured limestone rocks of the area, for which mean annual groundwater recharge up to 500 mm has been estimated [39]. Previous works [40–42] have indicated that in the strongly weathered upper part of the fractured limestones, denoted as epikarst [43], more permeable than the underlying carbonate rock, a perched aquifer might develop, ensuring the supply of springs and the recharge to deep groundwater through vertical conduits and fractures. This has been also reported for slopes in Campania with geomorphological characteristics similar to the one investigated in this study [44,45]. To deepen the knowledge about the hydrological processes involving the unsaturated pyroclastic deposits in response to meteorological forces, and to understand the water exchanges between the slope cover and the surrounding hydrological systems (i.e., with the atmosphere through the vegetation, with the groundwater through the soil–bedrock interface, with surface water circulation through overland and subsurface runoff) field monitoring can be very useful. Furthermore, field data can also help to distinguish the seasonal suction fluctuations related either to long-term or short-term response to meteorological forces [46,47]. Additionally, field monitoring can provide useful information that can help to build a mathematical model of the hydrological behaviour of the slope, which could predict the potential conditions of eventual landslide triggering [48–50]. Indeed, many field monitoring activities have been carried out on slopes subject to rainfall-induced shallow landslides, in most cases aimed at evaluating the pore water pressure fluctuations in the unsaturated soil covers in response to rainwater infiltration [46,51–56], without focusing on the hydrological interaction between soil and shallow bedrock and its influence on the potential triggering mechanism of landslides [57–59].

The goal of this paper is to analyse and discuss the hydrological processes involving the slope of Cervinara, around 40 km Northeast of Naples, in Campania (Southern Italy), considering their different scales and response times to precipitations, aiming at identifying the major hydrological processes that control the predisposing conditions of landslides, which can improve the predictive ability of models implemented in early warning systems. The studied slope was involved in catastrophic debris flow on 16 December 1999, triggered by a rainstorm of 325 mm in 48 h [60]. After that, hydrological monitoring activities have been carried out at the slope since 2002, initially consisting of measurements of rainfall depth and manual readings of soil suction about every two weeks [54]. The instrumentation has been integrated with further devices, and automatic acquisition and storage of the data were carried out from 2009 to 2012 [61,62]. In December 2017, new monitoring activities started, aimed at the assessment of the water balance of the slope, studying the interactions between the various hydrological systems

i.e., the unsaturated soil cover, the epikarst, and the underlying fractured limestone rock, which may affect the predisposing causes for the initiation of landslides along the slope.

2. Materials and Methods

2.1. Study Area

The study area is located near the small town of Cervinara, Northeast of Naples, in Campania (Southern Italy), along the slope of Mount Cornito (Figure 1).

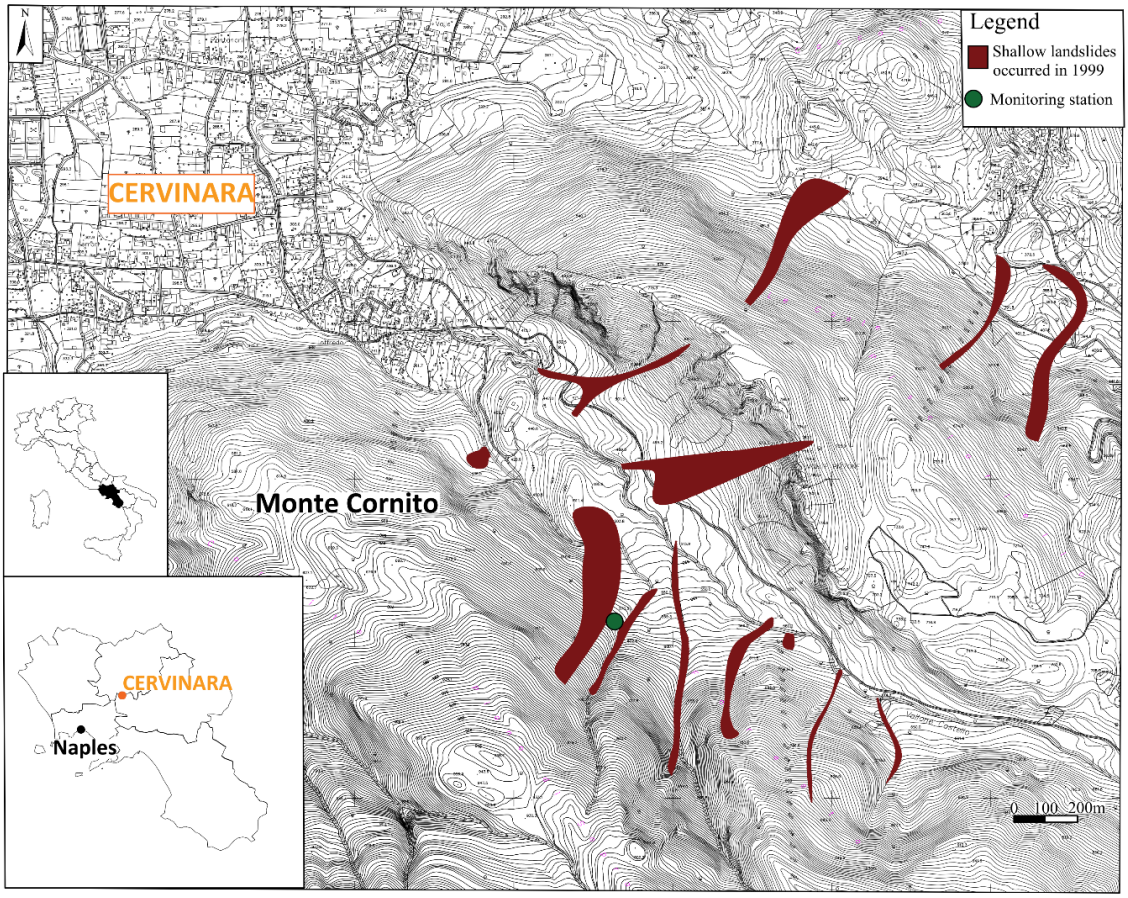

Figure 1. Map of the area around the slope of Cervinara with indication of the monitoring station and the areas affected by shallow landslides triggered by the rainstorm of 325 mm in 48 h of 16 December 1999.

The slope is covered with shallow deposits of pyroclastic materials generated from several eruptions of two main volcanic complexes of Campania, the Somma-Vesuvius and the Phlegrean Fields, which occurred during the last 40,000 years [63]. The soil cover, usually in an unsaturated condition, is mainly constituted by layers of volcanic ash of high porosity (up to 75%), and pumice lapilli, laying upon fractured calcareous bedrock. The total thickness of the cover is between 1.5 m and 2.5 m in the steepest part of the slope, while at its foot it reaches several meters [54]. The inclination of the slope ranges from 35° to 45° at an altitude between 500 m and 750 m. The climate of the area is Mediterranean, with the precipitation regime characterized by a dry season (from May/June to September), and a wet season (from October to the end of April/May). The mean annual precipitation in the area is around 1600 mm, and the total potential evapotranspiration ET_0, determined with the Thornthwaite formula, is between 700 mm (at the altitude of 750 m) and 800 mm (at 360 m) [48]. In the area, extreme daily rainfall heights of about 130 mm and 170 mm correspond to return periods of 10 and 50 years, respectively. The vegetation cover consists of cultivated chestnut trees (Castanea sativa). A dense

underbrush develops from late April to September, mainly formed by ferns (Pteridium aquilinum) and other seasonal shrubs.

2.2. Hydro-Meteorological Monitoring Station

Hydrological monitoring activities have been carried out at the slope of Cervinara since 2002, by measuring precipitation depth, soil water content and capillary tension [47,54]. Since December 2017, an automatic hydro-meteorological station has been installed at the altitude of about 585 m, immediately near the scarp of the 1999 landslide (Figure 1). The acquisition, with a time resolution of 1 h, and the data storage are ensured by a data logger, powered by a 12 V battery connected to two solar panels through a charge controller. Hydrological monitoring equipment includes five "Jet-fill" tensiometers equipped with tension transducers, a self-refilling tensiometer, and six probes for time domain reflectometry (TDR), connected through coaxial cables and a multiplexer to a reflectometer. The TDR probes are constituted by three metallic rods, with length of 0.10 m and diameter of 3 mm, spaced 1.5 cm apart. TDR is a widely used indirect technique for field measurements of soil water content [64], providing soil bulk dielectric permittivity, ε_r, which can be related to the soil volumetric water content, θ, through specific calibration expressions [65–67]. The meteorological station consists of a rain gauge with a resolution of 0.197 mm, thermo-hygrometer, soil temperature sensor, anemometer, pyranometer and barometric sensor. Table 1 summarizes the main characteristics of the installed devices. The solar panels and the meteorological sensors are fixed to a metal pole between 1.50 m and 2.50 m above the ground. The rain gauge is located on top of another metal pole, 2.00 m above the ground surface. Differently, the thermistor is buried under the soil surface at depth of 0.10 m (Figure 2).

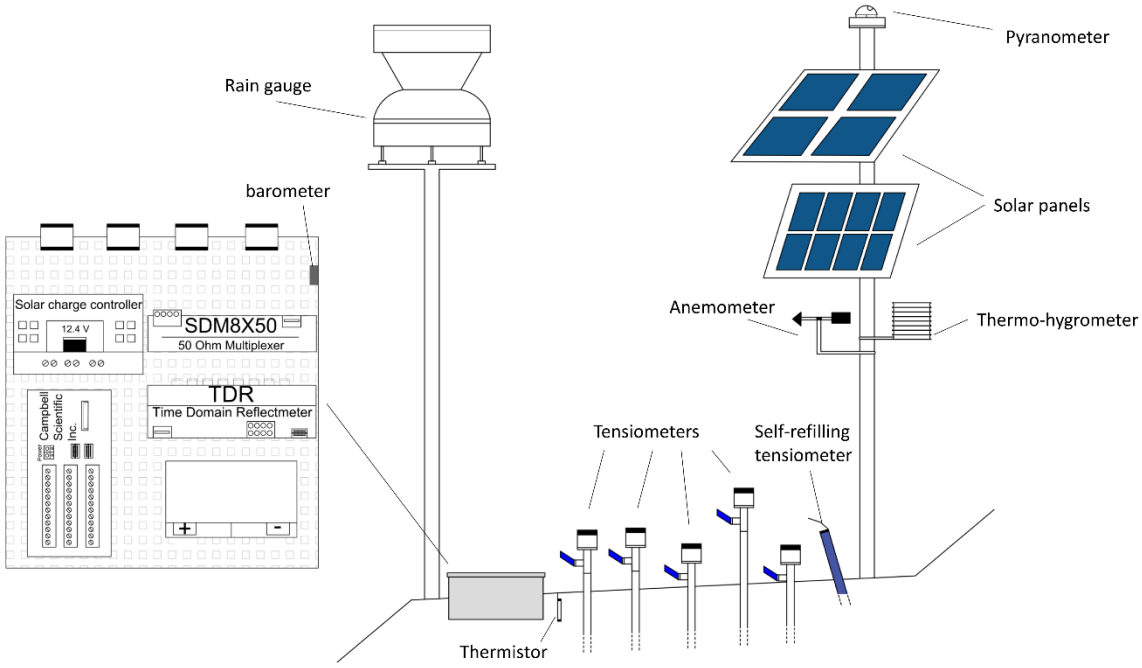

Figure 2. Schematic representation of the monitoring station.

Table 1. Main characteristics of the devices installed at the field monitoring station in Cervinara (* Campbell Scientific Inc., Logan, UT, USA; ** Soil Moisture Equipment Corp., Goleta, CA, USA; *** METER Group, Inc., Pullman, WA, USA).

	ELETRONIC SENSORS	COMPANY	MODEL	MEASUREMENT RANGE	TEMPERATURE RANGE	ACCURACY
1	Data logger and data Acquisition System	Campbell Scientific Inc. *	CR-1000	-	−25 °C to + 50 °C (standard)	± (0.06% of reading + offset) at 0 °C to 40 °C for Analog Voltage
2	Time- Domain Reflectometer	Campbell Scientific Inc. *	TDR-100	−2 m to 2100 m (distance) and 0 to 7 μs (time)	−40 °C to + 55 °C	-
3	Multiplexer for TDR System	Campbell Scientific Inc. *	SDM8 × 50	8-Channel	−40 °C to + 55 °C	-
4	Tension Transducer	Soil Moisture Equipment Corp. **	5301	0–85 cBar	0 °C to + 60 °C	0.25%
5	Self-refilling Tensiometer	METER Group, Inc. ***	TS1	0–85 kPa	−30 °C to + 70 °C	±0.5 kPa (Soil water tension) ±0.4 K (Temperature)
6	Rain gauge	Campbell Scientific Inc. *	ARG100	0–500 mm/hr	-	-
7	Thermo-hygrometer (Air Temperature)	Campbell Scientific Inc. *	CS215	−40 °C to + 70 °C	−40 °C to + 70 °C	±0.3 °C (25 °C) ±0.4 °C (5 °C to 40 °C) ±0.9 °C (−40 °C to +70 °C)
8	Thermo-hygrometer (Relative humidity)	Campbell Scientific Inc. *	CS215	0 to 100% (−20 °C to +60 °C)	−40 °C to + 70 °C	±2% (10% to 90% range) at 25 °C ±4% (0% to 100% range) at 25 °C
9	Thermistor	Campbell Scientific Inc.	107	−35 °C to +50 °C	−35 °C to + 50 °C	0.3 °C
10	Anemometer	Campbell Scientific Inc. *	WSS2	0–90 m/s	−20 °C to + 70 °C	2%
11	Pyranometer	Campbell Scientific Inc. *	SP110	0–1750 W/m^2	−40 °C to + 70 °C	±5%
12	Barometer	Campbell Scientific Inc. *	SB-100	15–115 kpa	−40 °C to + 125 °C	±1.5%

For the installation of the soil hydrological monitoring devices, a trench was excavated, and the TDR probes were horizontally pushed into its walls at various depths between 0.30 m and 2.00 m below the ground surface. Nearby, the tensiometers were installed vertically into the soil at the bottom of boreholes, previously excavated by a manual drill, between 0.20 m and 3.0 m below the ground surface.

From the top to the bottom of the soil cover, the following layers were found during the excavation: (i) layer A, organic top soil derived from volcanic ashes, with thickness of about 0.90 m; (ii) layer B, coarse pumices, about 0.40 m thick; (iii) layer C, volcanic ashes, about 0.20 m thick; (iv) layer D, fine pumices, with thickness of about 0.10–0.15 m; (v) layer E, volcanic ashes, more than 0.50 m thick. Unluckily, the total excavation depth (i.e., 2.15 m) did not allow to reach the underlying fractured calcareous bedrock. Figure 3 reports a schematic cross-section of the local stratigraphy with the location along the depth of the tensiometers and the TDR probes.

Disturbed samples were collected to retrieve the grain size distributions of the various layers, as shown in Figure 4.

The coarsest soil is the pumice layer B, which can be classified as gravel with sand, while the finest is the ash layer E, which is silty sand.

The ceramic tips of the tensiometers were located at depths of 0.20 m, 0.50 m, and 0.80 m in soil layer A, at 1.60 m (layer D) and at 1.80 m (layer E) of depth below the surface. The deepest one was located at 3.00 m of depth. The TDR probes were buried at depths of 0.30 m, 0.75 m, and 0.95 m in the shallowest layer (A), at 1.10 m in the coarse pumice layer (B), at 1.40 m in the volcanic ash layer (C), and, the last one at 2.00 m depth below the ground (layer E).

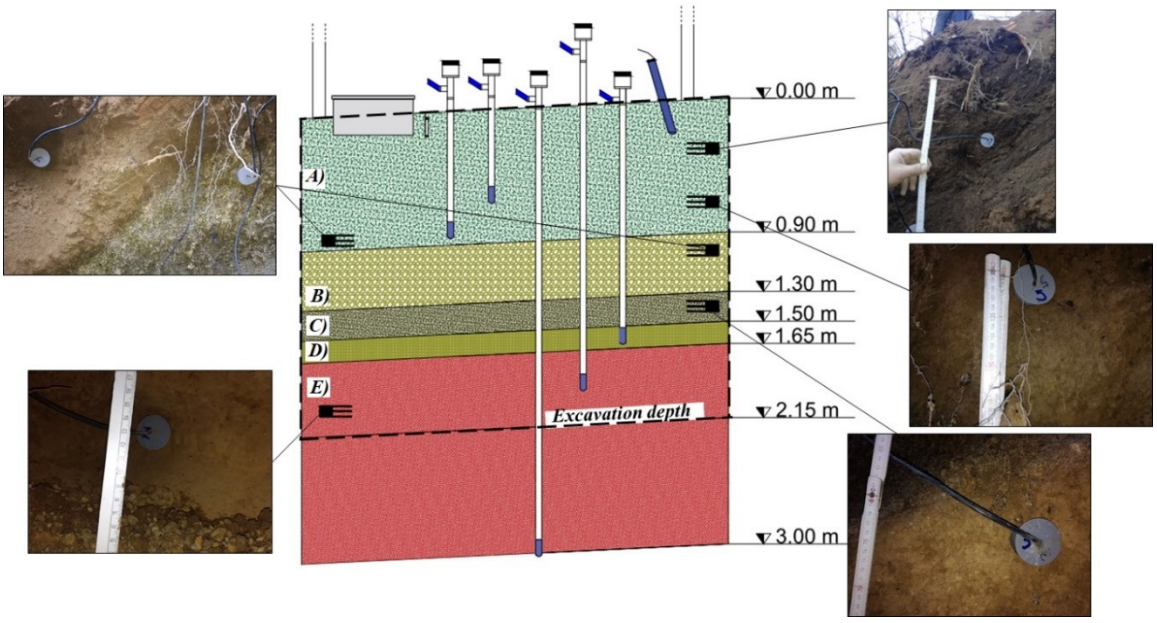

Figure 3. Sketch of the installed instruments (tensiometers and time domain reflectometry (TDR) probes) and of the soil profile at the field monitoring station. The stratigraphy: (i) organic topsoil (layer A); (ii) coarse pumices (layer B); (iii) volcanic ashes (layer C); (iv) fine pumices (layer D); (v) volcanic ashes (layer E).

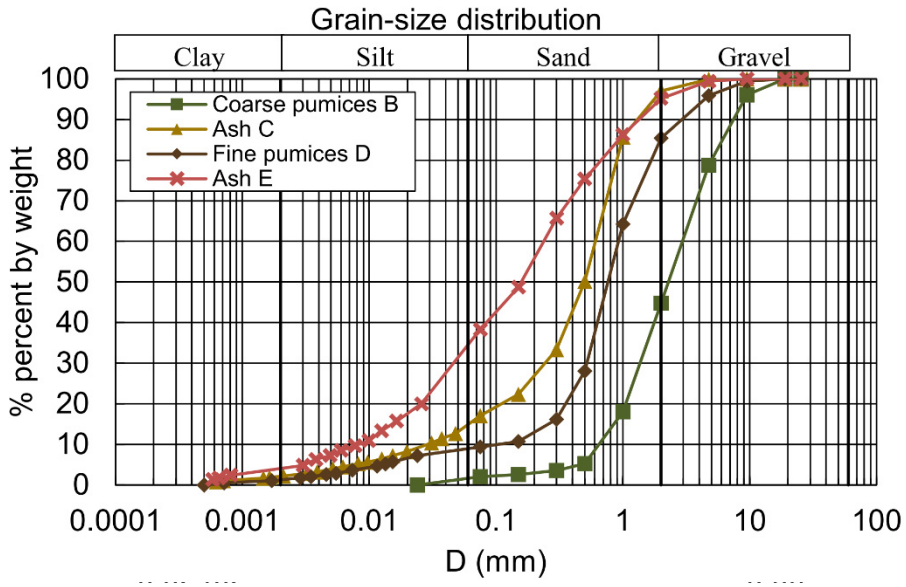

Figure 4. Grain-size distribution of the various layers.

2.3. Surface and Groundwater Circulation

In the surrounding area, a network of streams is present that intercept runoff and water from several ephemeral and perennial springs located in the surroundings (Figure 5, Table 2). The largest perennial springs, located at low elevations, are supplied by the deep groundwater system typical of the limestone massifs of the area [39]. Aiming at the assessment of the hydrological balance of the slope, the water levels of two streams located at the foot of the slope have been manually monitored every three or four weeks since December 2017 (Figure 5). Afterwards, in one of the two streams, located at 550 m a.s.l. (Section 1), a multiparameter probe, measuring water pressure, temperature and electrical conductivity, was installed in March 2019 to monitor the hydrologic regime of the stream with

a finer time resolution (one hour), and to identify the origin of the observed discharge, i.e., overland or subsurface runoff, or groundwater flow, which typically present electrical conductivities that differ more than one order of magnitude from each other [68–70].

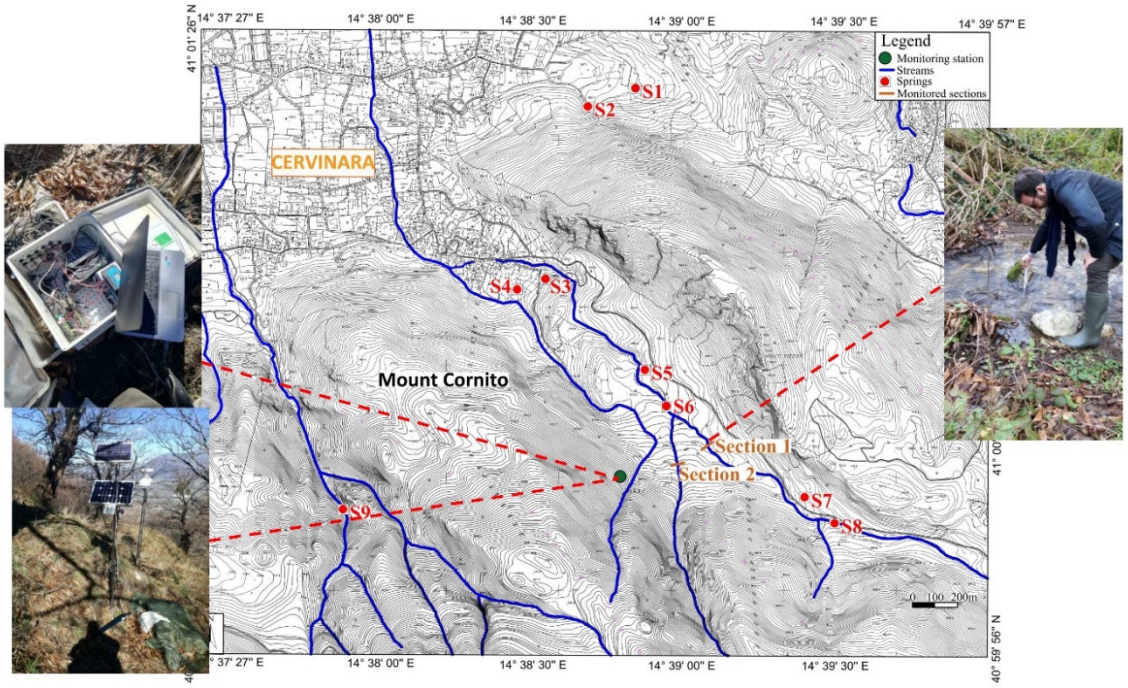

Figure 5. Map of the area around the slope of Cervinara with the location of the monitoring station and the main springs.

Table 2. Main springs in the area.

Number	Springs	Area	Regime
S1	Vullo	Valle	perennial
S2	Fontanastella	Valle	perennial
S3	Ricci	Castello	perennial
S4	Santospirito	Ioffredo	perennial
S5	Pastore	Castello	seasonal
S6	Acquerosse	Montepizzone	seasonal
S7	Pisciariello 1	Montepizzone	perennial
S8	Pisciariello 2	Foresta	perennial
S9	Livera	Piano Gregorio	seasonal

3. Monitoring Data

In this section, data from the field monitoring are described. Monitoring started on 7 December 2017 and is still ongoing. During this time, the monitoring has been quite continuous, except for three periods where the data logger was out of order. Moreover, the instrumentation was integrated with a thermo-hygrometer in May 2018. The collected data have been used to calculate the various terms of the water balance of the slope, consisting of the precipitation input, the stream discharge, the water exchanges with the atmosphere and with the deep groundwater system, and the water stored in the soil cover and in the perched aquifer temporarily developing in the upper part of the fractured limestone (epikarst).

3.1. Precipitations

Figure 6 shows the hourly rainfall recorded by the rain gauge during the monitored period.

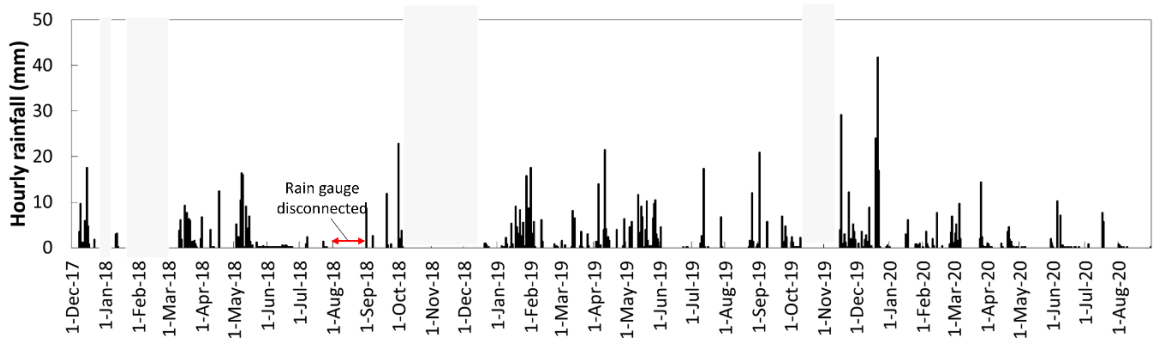

Figure 6. Monitoring data of recorded hourly rainfall (the grey shaded areas indicate periods with a lack of data).

Dry seasons, characterized by a few isolated rainfall events, usually start at the end of May and finish in September. Most precipitations fall between October and May. The most intense rainstorms occurred on 15 December 2017, and 20 and 21 December 2019. In the first case, 130 mm of rain fell, with a maximum hourly intensity of 18 mm/h. In the second case, 100 mm and 175 mm of rain were recorded in the two days, fallen after one and a half months of frequent precipitation (around 500 mm from the beginning of November until 19 December). After a maximum hourly intensity value of 41 mm/h occurred at 02:00 PM of 21 December, a shallow landslide was triggered along a slope about one kilometre far from the slope of Cervinara. It turned into a flowslide, and, after reaching the foot, it was channelized through a stream, reaching the nearby town of San Martino Valle Caudina. Moreover, the collected rainfall data are close in agreement with the data from the rain gauge of the regional Civil Protection Agency of Cervinara, not far from the monitoring area.

3.2. Evapotranspiration

To assess the hydrologic water balance accurately, actual evapotranspiration has to be estimated, based on the available meteorological data. The potential evapotranspiration has been estimated with the formulas of Hargreaves [71] (1), Blaney–Criddle [72,73] (2), with the Penman–Monteith equation [74] (3), and with the empirical formula of Thornthwaite [75] (4):

$$ET_0 = 0.0023\ (T_{mean} + 17.8)(T_{max} - T_{min})^{0.5} R_a \quad (1)$$

$$R_a = \frac{24\ (60)}{\pi} G_{sc} d_r [w_s sin(\varphi) sin(\delta) + cos(\varphi) sin(\delta) sin(w_s)]$$

In the previous equations, G_{cs} = 0.0820 MJ/m min represents the solar constant; d_r (m) is the inverse relative Earth–Sun distance; w_s (rad) is the sunset hour angle; φ (rad) is the latitude; δ (rad) is the solar radiation.

$$ET_0 = k(RH_{min}, U_z,\ r_i\ )\ [\ p\ (0.46\ T + 8)] - 2 \quad (2)$$

$$ET_0 = \frac{1}{\lambda}\left[86,400 * \frac{\Delta A + \frac{\rho_a c_p D}{r_a}}{\Delta + \ \gamma\left(1 + \frac{r_s}{r_a}\right)}\right] \quad (3)$$

$$ET_0 = \ 16\left(\frac{L}{12}\right)\left(\frac{N}{30}\right)\left(\frac{10T_\alpha}{I}\right)^\alpha \quad (4)$$

$$\alpha = \left(6.75 * \ 10^{-7}\right)I^3 - \left(7.71 * \ 10^{-5}\right)I^2 + \left(1.792 * \ 10^{-2}\right)I + 0.49$$

$$I \ = \ \sum_{i=1}^{12}\left(\frac{T_{ai}}{5}\right)^{1.514}$$

In the previous equations, I is the heat index, which depends on the mean monthly temperatures T_{ai} (°C). In this case, as no continuous temperature data were collected, the monthly temperatures

recorded between 1989 and 1999 from Montesarchio station (560 m a.l.s), about 10 km from Cervinara, were used. In Table 3, the parameters required by Equations (1)–(4) are summarized.

Table 3. Summary of the parameters (determined using the meteorological data collected by the Cervinara station or from literature or evidence on site).

1. Hargreaves (mm/day)		
T_{mean} = mean daily air temperature	(°C)	*
R_a = extraterrestrial radiation	(mm/day)	-
2. Blaney–Criddle (mm/day)		
RH_{min} = daily minimum relative humidity	(%)	*
U_z = daily wind speed at 2 m above the ground	(m/s)	*
r_i = ratio between monthly average daily bright sunshine duration n(h) and monthly average maximum daily sunshine duration $N(h)$	(-)	0.7
p = mean daily percentage of annual daylight hours for a given month	(%)	$\left(\frac{N}{4380}100\right)^{**}$
T = mean monthly air temperature	(°C)	*
3. Penman–Monteith (mm/day)		
λ = latent heat of vaporisation of water	(MJ/kg)	2.45
Δ = slope of the saturation vapor pressure-temperature relationship, de_s/dT	(kPa/°C)	$\frac{4098\left(0.611\exp\frac{17.27\ T^*_{mean}}{(237.3+T^*_{mean})}\right)}{(273.3+T^*_{mean})^2}$
T_{mean} = mean daily air temperature	(°C)	*
A= Available energy		R_n-G–P
R_n = net radiation flux	(MJ/m^2 day)	(1–α) R*
G = soil heat flux		-
P = energy absorbed by biochemical process in the plants		2% R_n
ρ_a = density of moist air	(kPa/m^3)	$3.486\frac{Patm^*}{(275+T^*_{mean})}$
c_p = specific heat of moist air	(MJ/kg °C)	0.001013
D = vapour pressure deficit	(kPa)	$e_s - e_a$
e_s = mean saturated vapor pressure	(kPa)	$0.611\exp\frac{17.27\ T^*_{mean}}{(237.3+T^*_{mean})}$
e_a = mean actual vapor pressure	(kPa)	$\frac{RH^*_{mean}}{100}e_s$
γ = psychometric constant	(kPa/°C)	$0.000665\ Patm^*$
rs = surface resistance to vapor emission by the stomata of leaves	(s/m)	$200/(LAI)$
ra = aerodynamic resistance to upward vapor diffusion	(s/m)	$\frac{\ln\left[\frac{(z_u-0.67\ h_c}{0.123\ h_c}\right]^2}{0.168\ U^*_z}$
z_u = elevation of wind speed measured	(m)	2
h_c = vegetation height	(m)	18
4. Thornthwaite (mm/month)		
T_a = average daily air temperature for a given month	(°C)	***
L = monthly average maximum daily bright sunshine duration	hour	**
N = number of days for a given month	(-)	

* data from the meteorological station of Cervinara; ** data from latitude area, 41° North; *** data from the meteorological station of Montesarchio (560 m a.l.s), about 10 km from Cervinara.

The leaf area index (LAI), required for the calculation of ET_0 with Penman–Monteith Equation (3), has been assumed equal to 4 m^2/m^2 between May and August when foliage and dense underbrush are present (as indicated by [76,77] for Italian *Castanea Sativa*), while it has been considered negligible from November to February, when the trees are leafless. Smaller values have been assumed when foliage and underbrush are not fully developed, namely 1.5 m^2/m^2 in March and October, and 3 m^2/m^2 in April and September. The tree height has been assigned equal to 18 m through visual inspection, in agreement with [78]. Moreover, as the magnitude of daily soil heat flux G over a period of 10–30 days is very small compared to net radiation flux, R_n, it has been neglected [79]. The short-wave radiation reflection

coefficient α (albedo) has been considered equal to 0.23 according to vegetation cover type [79,80]. Figure 7 reports the average monthly potential evapotranspiration rate estimated by Equations (1)–(4).

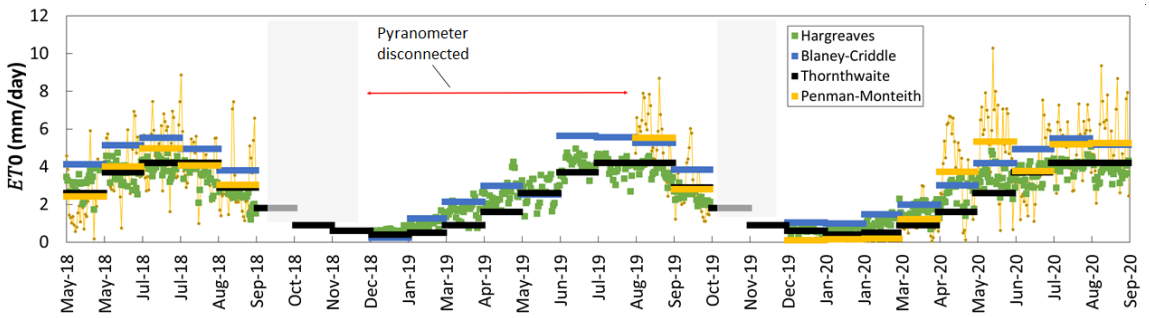

Figure 7. Mean monthly potential evapotranspiration rate estimated with different formulas (mm/day). To help with comparison among different formulas, both daily and monthly-averaged data by Penman–Monteith equation are given (the grey shaded areas indicate periods with a lack of data).

The main pro of using the simple formulas of Hargreaves (1) and Thornthwaite (4) is the minimum data requirement, i.e., only air temperature data are needed. However, the application of the Blaney–Criddle formula (2) and Penman–Monteith Equation (3) provides more reliable estimates, as both take into account the effects of actual insolation time (ratio n/N between actual and maximum possible bright sunshine hours) and all the measured meteorological variables, while the latter also allows combining them with the estimates of stomatal resistance to evapotranspiration by vegetation. The potential evapotranspiration values estimated by Penman–Monteith and Blaney–Criddle equations are in many months larger than the ones provided by expressions (1) and (4), especially from April to September, with the highest evapotranspiration rate (10 mm/day) calculated in May 2020. Indeed, the three monitored years were much warmer than the average. The lowest estimated evapotranspiration rates, namely 0.02 mm/day and 0.1 mm/day, respectively, in December 2019 and January 2020, confirm the interplay of the absence of foliage and underbrush with low solar radiation during the winter season [73,81]. To consider the specific climatic features of the monitoring years, the monthly values of ET_0 from the Blaney–Criddle formula have been adopted for the assessment of the water balance, except for the periods where the meteorological station was out of order—when the mean estimates of Thornthwaite formula have been used. Indeed, the Penman–Monteith equation suffered from too long periods where there was a lack of data due to the discontinuous functioning of the pyranometer (Figure 7). To obtain actual evapotranspiration ET, the estimated ET_0 must be multiplied by a crop coefficient, depending on the characteristics of the vegetation and on the climatic conditions. The suction measurements (Section 3.4) indicate that the soil only rarely became so dry it induced stress to the vegetation (i.e., this could have occurred only sporadically from late July to September). In this period, ET can therefore be assumed close to potential evapotranspiration ET_0. Conversely, the dormant vegetation implies that in autumn and winter ET is likely quite smaller than ET_0. Hence, the crop coefficients have been assumed between 0.3 (from December to February) and 0.9 (from May to July). The estimated annual ET_0 and ET are reported in Table 4.

Table 4. Estimated annual potential evapotranspiration ET_0 and actual evapotranspiration ET.

Year	ET_0 (mm)	ET (mm)
2017–2018	911.3	734.3
2018–2019	1000.3	781.0
2019–2020	1021.6	793.2

3.3. Stream Discharges

Figure 8 shows the manually measured water levels in the two monitored stream sections—1 and 2 (Figure 5).

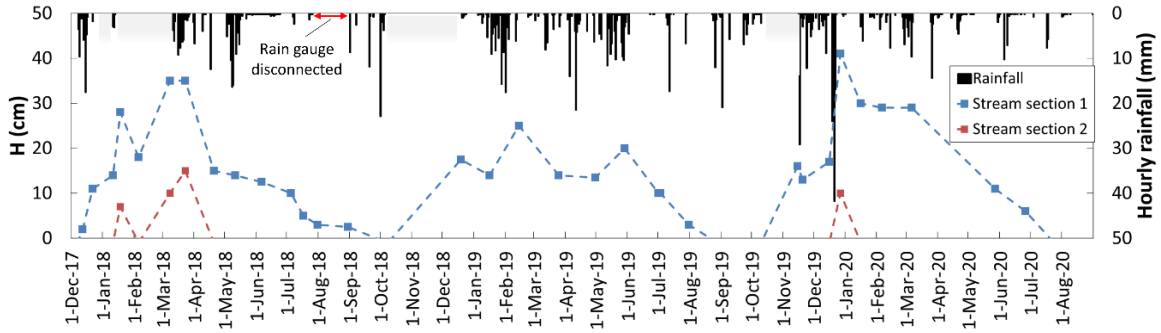

Figure 8. Measured water levels in the two monitored sections and monitoring data of recorded rainfall (the grey shaded areas indicate periods with a lack of data).

The water level in stream Section 1, located at lower altitude than Section 2, starts growing in autumn (i.e., between late September and early December, depending on the year), and reaches its maximum between late winter and early spring. In late spring and summer, the water level progressively decreases, and the stream becomes dry in late summer. In Section 2, instead, water flow has been observed only sporadically, after extremely rainy periods. Given the small extension of the catchments of the two sections, the delay and persistence of the water level variations, compared to the precipitation, seem to indicate that the discharge in the streams cannot be considered as the result of surface or subsurface runoff. To estimate the stream discharge Q_s [L/T] from the water level readings H [L] reported in Figure 8, a monomial stage–discharge relationship has been defined for each hydrological year:

$$\frac{Q_s}{Q_{max}} = \left(\frac{H}{H_{max}}\right)^{\alpha} \quad (5)$$

where H_{max} and Q_{max} represent the maximum water level, and the corresponding estimated flow discharge, and α [-] is an exponent assumed to be equal to 2.5. The maximum flow discharge value has been estimated by measuring the cross-sectional area and evaluating the mean flow velocity. Figure 9 reports the estimated discharges of the two monitored streams.

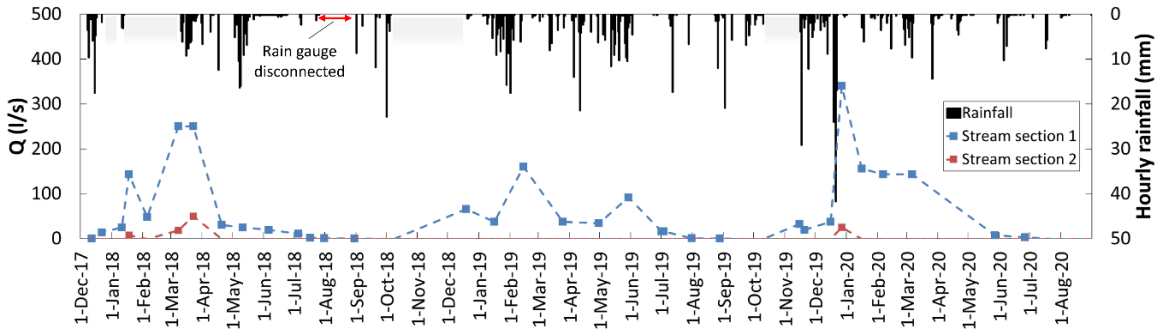

Figure 9. Estimated flow discharges of the two monitored stream sections (the grey shaded areas indicate periods with a lack of data).

Figure 10 shows the water level and electrical conductivity in stream Section 1 (Figure 5), measured by the multiparametric probe between April 2019 and August 2020.

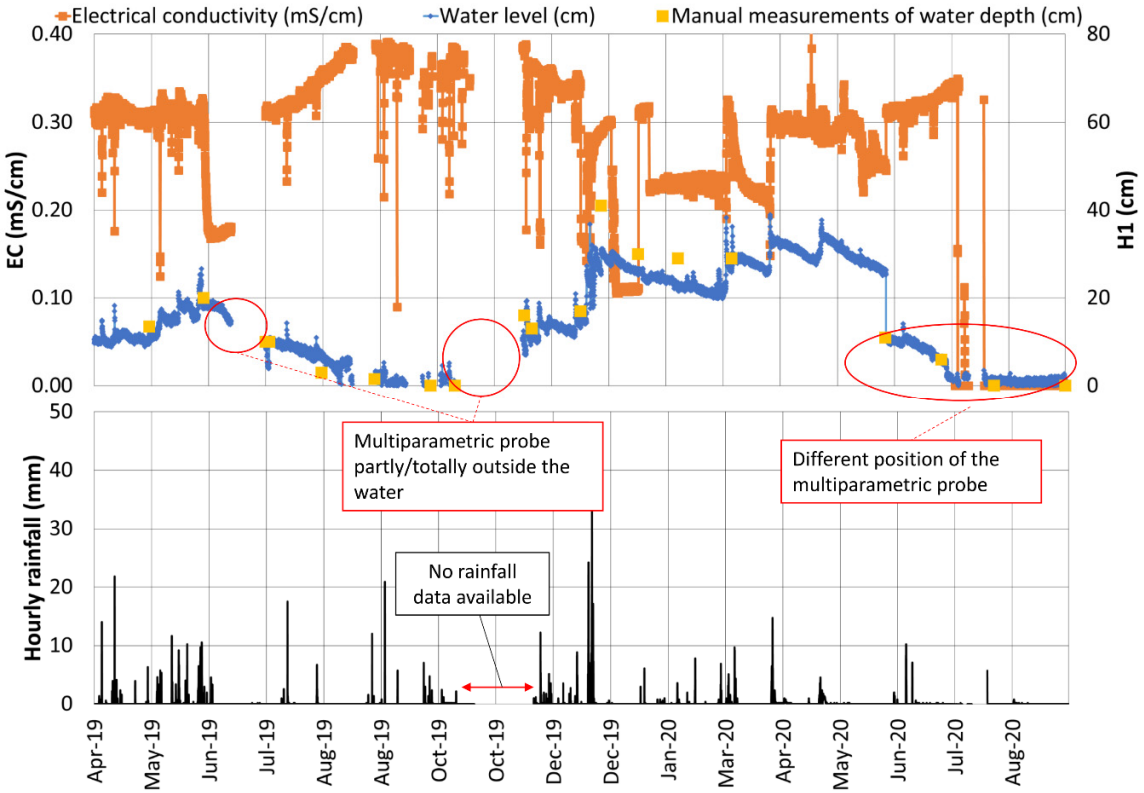

Figure 10. Rainfall depth, electrical conductivity, and water depth measured by the multiparametric probe.

The values of electrical conductivity are mostly between 0.2 and 0.4 mS/cm, confirming that the stream discharge is likely originated by baseflow and not by surface runoff, which would be associated with electrical conductivity two orders of magnitude smaller [69]. During rain events, when the water level peaks, the electrical conductivity quickly decreases, indicating that rainwater mixes with the water flowing through the stream. Some large rainfall events have been chosen to infer the importance of overland and subsurface runoff in the observed discharge generation (Figure 11). Specifically, for each event, runoff coefficients *C* [-] have been estimated as the ratio between total specific flood runoff volume (calculated on the basis of the area between the dashed lines, indicating the estimated baseflow trend, and the total discharge line in the graphs of Figure 11) and the precipitation depth of each event (Table 5).

Table 5. Runoff coefficients estimated for several events.

Event	Data	Total Precipitation Depth (mm)	Total Specific Flood Runoff Volume (mm)	Runoff Coefficient (%)
(a)	15 May 2019	45.1	0.487	1.08
(b)	27 May 2019	25.6	0.253	0.98
(c)	24 November 2019	34.5	0.217	0.63
(d)	13 December 2019	35.3	0.197	0.56
(e)	19 December 2019	102.2	1.038	1.02

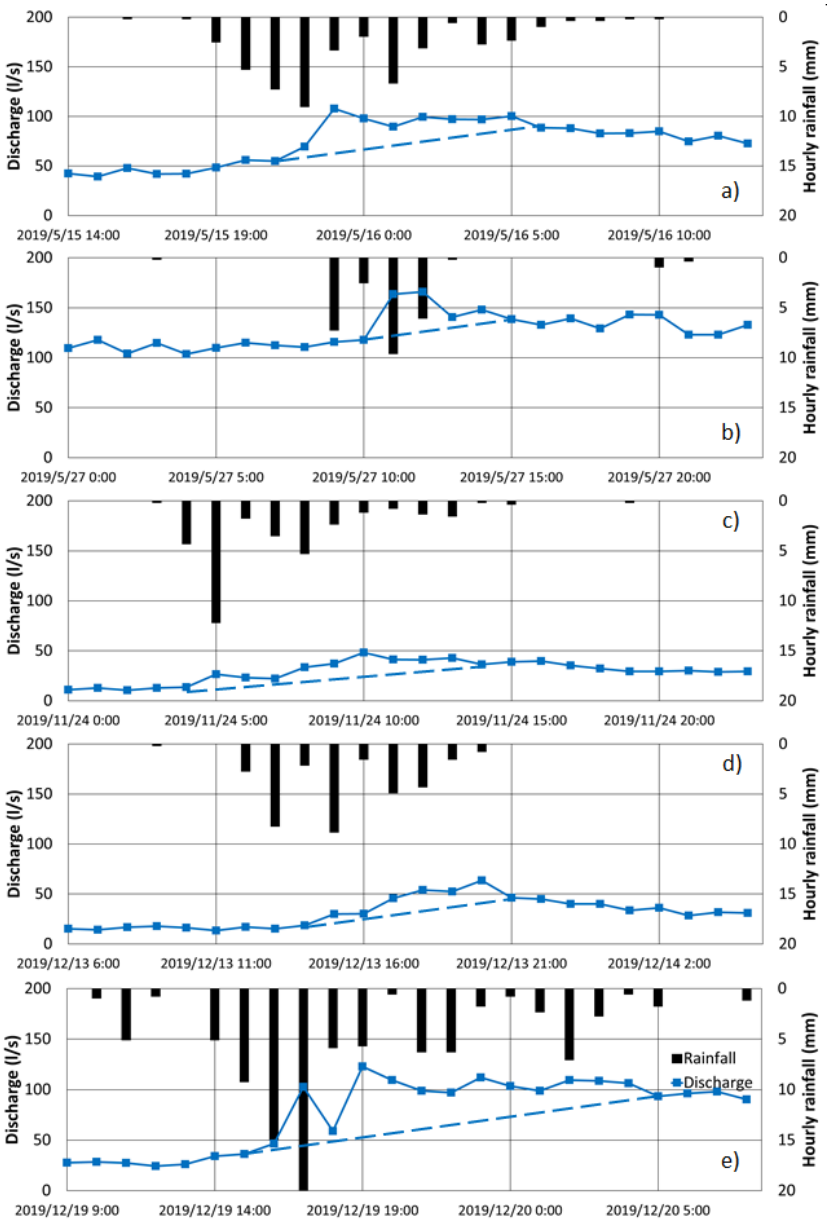

Figure 11. Stream response of events: 15 May 2019 (**a**); 27 May 2019 (**b**); 24 November 2019 (**c**); 13 December 2019 (**d**); 19 December 2019 (**e**); the dashed lines represent the estimated baseflow trends during the events.

The values reported in Table 5 indicate that the runoff coefficients are in all cases very small, although the selected events are among the largest occurred during the monitoring period. In fact, just a small discharge growth during rainfall is observed, while a stable increase is established after the end of each event, which can be interpreted as a relatively fast baseflow. During rainfall events smaller than the selected ones, no significant increase was observed.

Consequently, the response of stream discharge to precipitations seems mostly supplied by baseflow, which, given the relatively fast response, can be related to groundwater circulation occurring in the shallower part of the limestone bedrock. Hence, both overland and subsurface runoff contributions can be neglected in the assessment of long-term water balance.

3.4. Soil Water Content and Suction

Figure 12 shows, from top to bottom panels, the hourly rainfall, soil water and suction measurements during the monitored period.

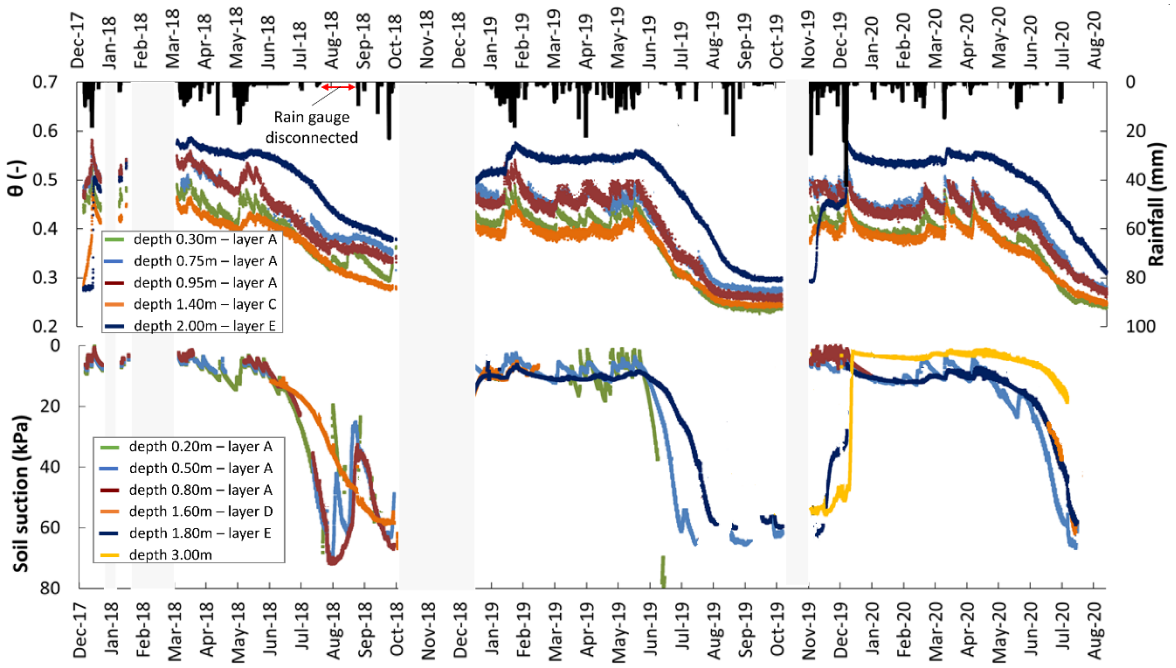

Figure 12. Monitoring data of recorded hourly rainfall, soil water content and suction at various depths between December 2017 and August 2020 (the grey shaded areas indicate periods of lacking data).

Despite the lack of data during the autumns in 2018 and 2019, it is possible to recognize seasonal suction fluctuations characterized by trends similar to those observed in other pyroclastic covers in Campania [46,82,83]. Specifically, suction values in the deepest layer always remained lower than that recorded in the uppermost part of the cover, with the exception of short periods during the rainy seasons, when the rainwater infiltration did not yet affect the deepest part of the cover. Furthermore, given the very high porosity of the deposit (i.e., up to 0.75 for the ashes) and the mean water content recorded during the wet seasons, which never exceeded 0.50, the soil was always far from saturation. Figure 13 shows the soil response in terms of water content and suction observed during the wet period (25 March–30 April 2019, characterized by a total rainfall depth of 123 mm).

The effects of infiltration in response to rainfall generally depend on depth, as fluctuations of soil water content and suction are delayed and smoothened (less marked) in the deepest layers, while in the shallowest ones, they tend to be rapid and higher (values of suction decrease quickly and immediately after the observed rainfall). Figure 14 shows the soil response observed during the dry period (1 June–31 July 2019).

In this case, it is easy to note that the suction starts to increase earlier and faster in the shallowest layers, and then in the deepest ones. This response can be related to the upward evapotranspiration fluxes due to the water uptake from the roots, which are denser in the upper part of the soil cover due to the flourishing underbrush. Although the soil moisture dynamics are strictly connected to the specific precipitation trends of each hydrologic year, it is possible to define different periods with a similar profile in terms of soil water content and suction (Table 6).

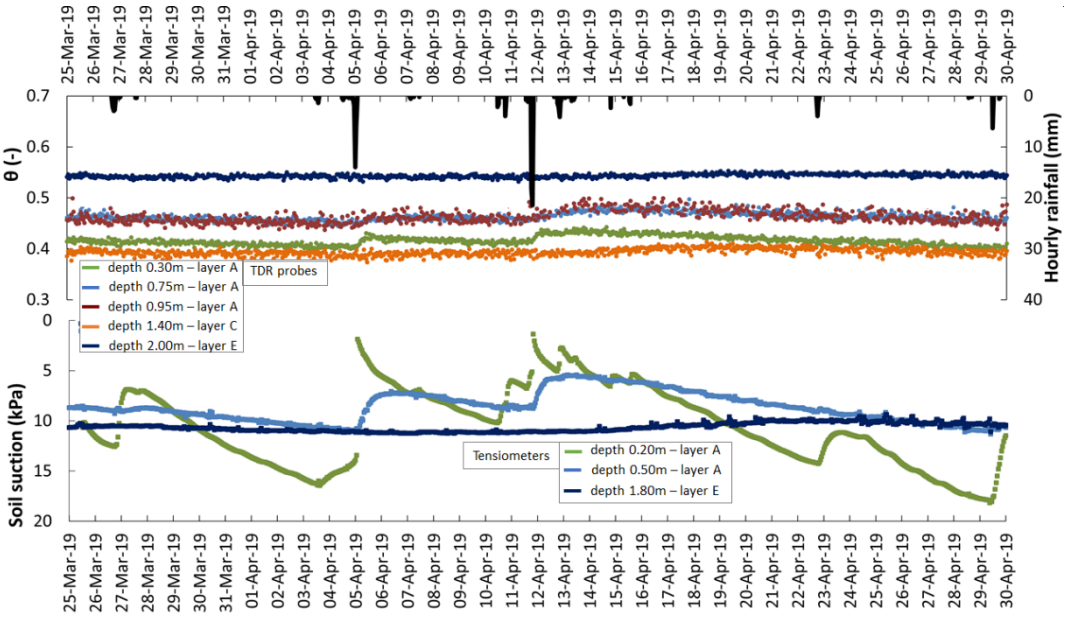

Figure 13. Measurements of hourly rainfall, water content and suction from 25 March to 30 July 2019.

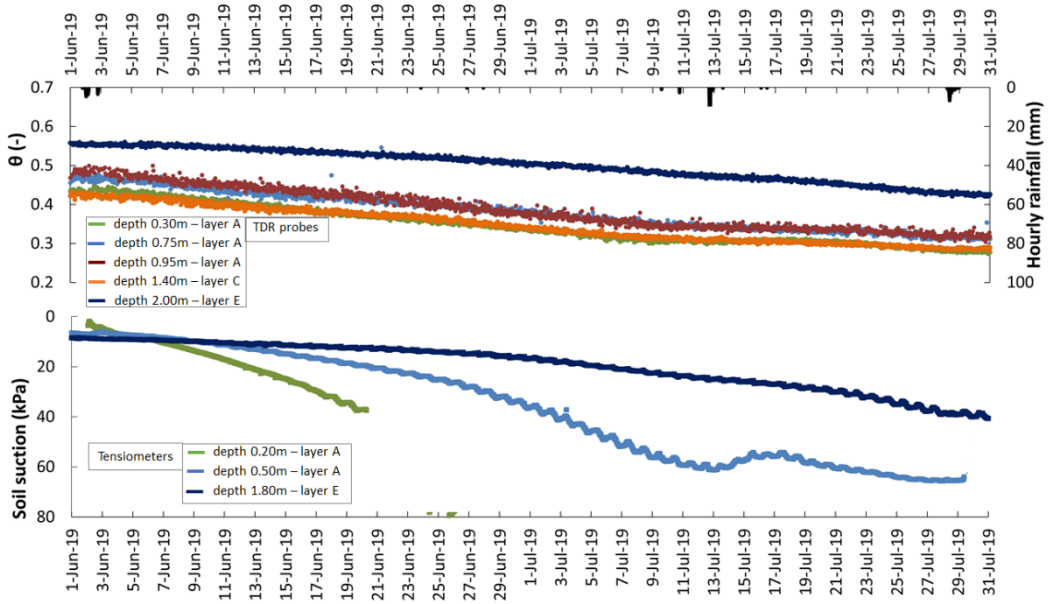

Figure 14. Measurements of hourly rainfall, water content and suction from 1 June to 31 July 2019.

Table 6. Periods with similar hydrological behaviour.

Months	Oct	Nov	Dec	Jan	Feb	Mar	Apr	May	Jun	Jul	Aug	Sep
Seasons *				wet						dry		
This study **		Late autumn [1]			Middle winter [2]				Late spring [3]		Summer end [4]	

* As observed by rainfall data in Figure 6, the dry seasons start at the end of May and finish in September.
** Typical profiles observed in this study (see Figure 15): [1] moisture strongly increasing upward, [2] moisture evenly high, [3] moisture decreasing upward, [4] moisture evenly low.

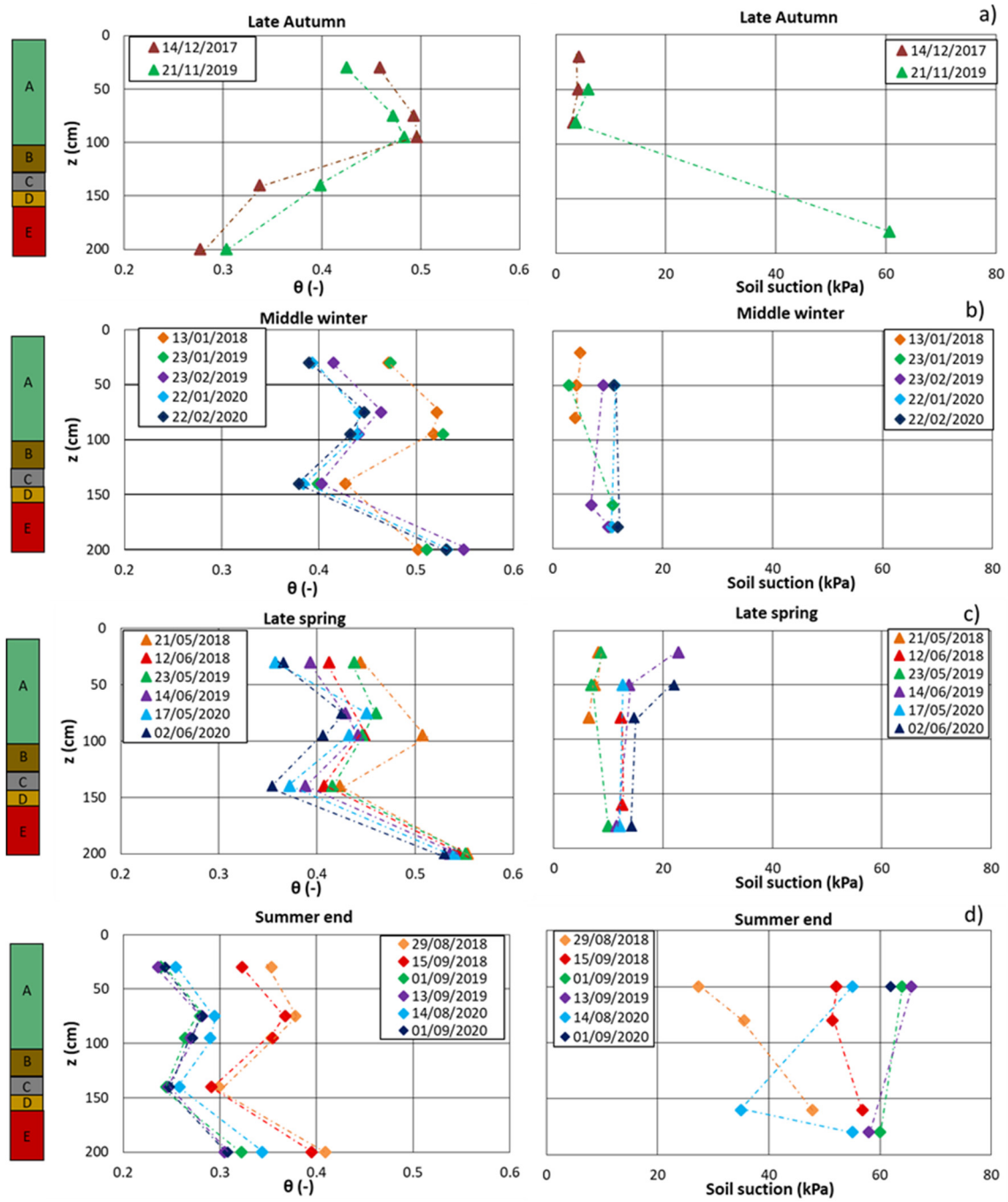

Figure 15. Water content and suction profile in soil cover during different periods: late autumn (**a**); middle winter (**b**); late spring (**c**); summer end (**d**).

Figure 15 shows soil water content and suction profiles throughout the soil cover, estimated from the local values at the depths where TDR probes and tensiometers were located, in late autumn, middle winter, late spring and summer from 2017 to 2020.

In late autumn (Figure 15a), the slopes are being rewetted in the upper part (layer A) after the typical dry and hot Mediterranean summer, as the wetting front in response to rainfall is not still able to propagate to further depths (only the shallowest layer has a quick response to precipitation). In these cases, the water content and suction in superficial levels of soil (layer A) reach values between 0.42–0.50 and 5–8 kPa, respectively. On the other hand, during the middle of winter (Figure 15b), the prolonged rainy periods allow the rainwater infiltration to reach the deepest layer (layer E), leading to a relatively uniform wetting of the entire thickness of the pyroclastic cover, with water content ranging between

0.38 and 0.55 and the correspondent suction ranging between 2–3 kPa in the uppermost part and about 15 kPa at greater depth. The base of the soil profile becomes wet, indicating that in this period gravitational leakage from the soil profile may occur. In the late spring (Figure 15c), the soil profile starts being progressively dried, mostly in the uppermost meter, due to the water uptake from the growing vegetation. In fact, the water content ranges between 0.35 and 0.45 (with an exceptional case of 0.5 during 2018) and suction between 8 kPa and 22 kPa. At the base of the profile (layer E), the soil is still wet given the slower downward-directed gravitational drainage towards the underlying fractured bedrock. At the end of summer (Figure 15d), after a prolonged dry period (with only a few isolated summer rainstorms), the soil profile becomes evenly dry. The values of suction reach 60 kPa, while the water content drops below 0.3 (except during 2008).

4. Discussion

The measured precipitation and soil water content, and the estimated evapotranspiration and stream discharges, have been used to assess the water balance of the hydrological system along three hydrologic years, between 1 September 2017 and 31 August 2020 (Figure 16):

$$\int_0^t (R - ET - q_s)\, dt = V_s + V_b \tag{6}$$

At the right hand side of Equation (6), written in terms of specific storage [L], V_s and V_b represent the water volume stored in a column of unit area of soil and bedrock (epikarst and groundwater system), respectively. At the left hand side, R is rainfall intensity [L/T], ET is the actual evapotranspiration [L/T], and q_s is the specific stream discharge [L/T]. The various terms of Equation (6), cumulated over each monitored hydrological year, are plotted in Figure 16. The measured precipitations were used to assess the rainfall intensity R. During the periods where the rain gauge was out of order (Section 3.1), the data were supplemented with those collected by the nearby rain gauge of Cervinara, managed by the regional Civil Protection Agency, located at the foot of the slope. The empirical formula of Blaney–Criddle was used to estimate the evapotranspiration ET (Section 3.2). The total discharge (sum'of estimated discharges of the two monitored streams, Section 3.3) was divided by the underground watershed extension, estimated around 2.5 km^2 from the geologic map of the area, to obtain the specific discharge q_s. The measurements of soil water content, obtained by the TDR probes installed at depths of 0.30 m, 0.95 m, 1.40 m and 2.00 m (Section 3.4), allow the estimation of soil specific storage ($V_s = \sum \theta_i \Delta z_i$) in the whole soil cover, for which the total thickness was assumed to be equal to 2.60 m. Finally, the term V_b was obtained from the other measured/estimated terms with the balance Equation (6). To help understand the annual dynamics of the water balance, in Figure 16 both the specific storage terms V_s and V_b have been set to zero at the beginning of each hydrologic year.

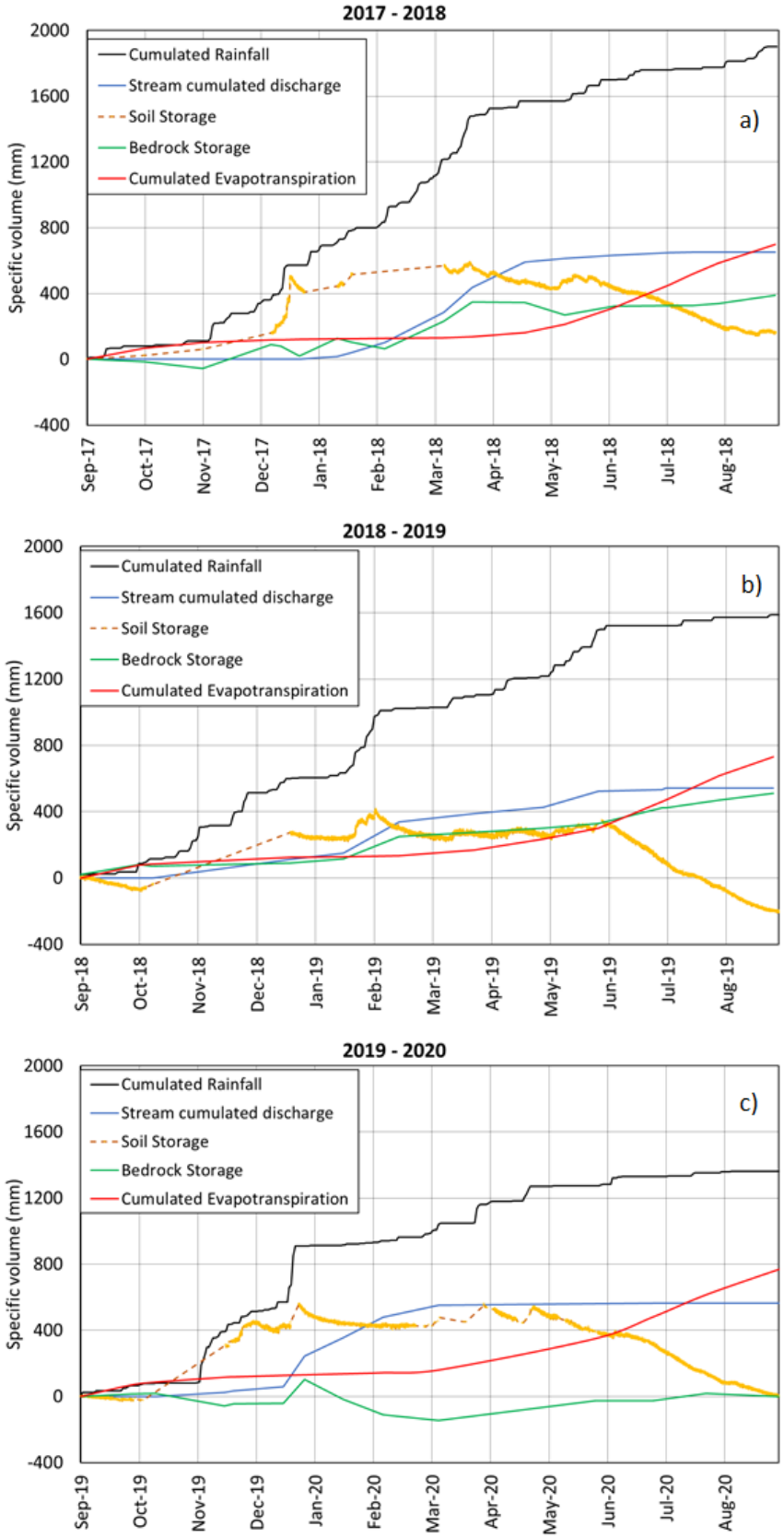

Figure 16. Specific water balance of the slope estimated from monitoring data: 1 September 2017 and 31 August 2018 (**a**); 1 September 2018 and 31 August 2019 (**b**); 1 September 2019 and 31 August 2020 (**c**); note that the storage terms V_s and V_b are set to zero at the beginning of each hydrologic year.

From the yearly trend of the various terms of the water balance, it is clearly shown how the monitored streams are almost dry from the end of summer until nearly the end of the year. Afterwards, the shallow groundwater circulation supplying the streams becomes active, with maximum discharge in early April (17–18), in February (18–19), in December (19–20), and returning to dry in September (2018) and in August (2019 and 2020). The slow response of the stream to precipitation indicates that part of the water is temporarily stored within the epikarst, before coming out into the streams. From the plots of Figure 16, it clearly seems that stream discharge appears when water starts to be stored in the fractured bedrock. As the soil cover remains far from saturation during the entire rainy season (from October to April/May), a condition not favouring fast lateral subsurface flow through the soil cover, the stream water likely originates from the upper part of the fractured bedrock, where a temporary perched aquifer likely develops. It is also worth noting the different response of the soil cover to precipitation in different periods of the rainy season. In fact, soil storage strongly increases only in late autumn and early winter, being nearly equal to the total precipitation (e.g., December 2017 and November 2019) and indicating that little water reaches the fracture bedrock in this period of the year, probably limited by the still dry lower part of the soil cover. Afterwards, although significant precipitation normally occurs during the whole of winter and early spring, soil storage exhibits small fluctuations around values still far from saturation (e.g., March 2018, February–May 2019 and April 2020). As evapotranspiration is limited in this period of the year, it can be argued that most infiltrating water crosses the soil cover and reaches the underlying fractured bedrock. Hence, the transfer of water from the soil cover to the fractured bedrock appears an important process to prevent the achievement of high moisture conditions within the soil cover. This result can help understand why many landslides have been recorded in late autumn and early winter in Campania [48,49].

5. Conclusions

To investigate the hydrologic behaviour of an unsaturated pyroclastic slope cover laying upon a fractured limestone bedrock in response to meteorological forces, an automatic meteo-hydrological monitoring station was installed along the slope of Cervinara, Northeast of Naples, where catastrophic rainfall-induced landslides occurred in December 1999. The acquired set of data, consisting of rainfall input, meteorological variables, stream discharge, and water contents of the soil cover, enabled the assessment of the water balance of the slope for three hydrological years (2017–2018, 2018–2019, 2019–2020) and, in particular, the terms of water storage in the soil cover and in the fractured bedrock, and the exchanges of water with the atmosphere, through actual evapotranspiration, and with the epikarst and the deeper groundwater system through leakage at the bottom of the soil cover. The comparison between the times of generation of the stream discharge and of the bedrock storage suggests that a perched aquifer temporarily develops in the epikarst once the soil cover has become wet. In fact, the leakage from the soil cover to the perched aquifer seems to be related to the moisture conditions at the base of the soil profile, which exhibit recurrent seasonal behaviour. Specifically, varying soil response in terms of water content and suction during wet and dry seasons is observed, and four different periods with recurrent similar soil profiles are defined, i.e., late autumn, middle winter, late spring and summer end.

The observed recurrent soil moisture conditions in early winter can be of use to understand why many landslides occur in this period in Campania. In fact, the still dry conditions of the lowermost part of the soil cover, as well as the still poor accumulation of water in the epikarst, hamper the drainage through the soil–bedrock interface, and thus favouring the fast accumulation of water within the cover during rainfall events, which can eventually lead to slope failure.

The obtained results, while confirming that, in the studied geomorphological context, soil moisture monitoring can be of great help for the improvement of landslide prediction, also indicate that other variables, such as stream water level, can be a proxy of the hydrological conditions, which can predispose the slopes to landslides. This can be of help for the development of effective landslide early warning systems, simple enough to be operated by public authorities in charge of civil protection actions.

Author Contributions: Conceptualization, E.D., R.G. and P.M.; methodology, R.G. and P.M.; validation, E.D. and R.G.; investigation, L.C., E.D., R.G., P.M. and L.O.; data curation, P.M.; writing—original draft preparation, P.M.; writing—review and editing, E.D. and R.G.; supervision, E.D. and R.G.; funding acquisition, R.G. All authors have read and agreed to the published version of the manuscript.

Funding: This research was funded by Università degli Studi della Campania "L. Vanvitelli" as part of the Ph.D. project "Modelling hydrological processes affecting rainfall-induced landslides for the development of early warning systems" within the Doctoral Course "A.D.I.". Experimental activities were also funded by Università degli Studi della Campania "L. Vanvitelli" through the programme "VALERE: VAnviteLli pEr la RicErca".

Acknowledgments: The authors acknowledge Luciano Picarelli, who inspired this research and provided useful comments and advice throughout its entire development.

Conflicts of Interest: The authors declare no conflict of interest.

Data Availability: The complete data collected by the meteorological station since 2017, including soil and air temperature, relative humidity, solar radiation, atmospheric pressure, and wind speed, may be kindly requested from the authors.

References

1. Bogaard, T.A.; Greco, R. Landslide hydrology: From hydrology to pore pressure. *Wiley Interdiscip. Rev. Water* **2016**, *3*, 439–459. [CrossRef]
2. Wieczorek, G.F.; Glade, T. Climatic factors influencing occurrence of debris flows. In *Debris-Flow Hazards and Related Phenomena*; Springer: Berlin/Heidelberg, Germany, 2007; pp. 325–362.
3. Bogaard, T.A.; van Asch, T.W.J. The role of the soil moisture balance in the unsaturated zone on movement and stability of the Beline landslide, France. *Earth Surf. Process. Landf.* **2002**, *27*, 1177–1188. [CrossRef]
4. Terlien, M.T.J. Hydrological landslide triggering in ash-covered slopes of Manizales (Columbia). *Geomorphology* **1997**, *20*, 165–175. [CrossRef]
5. Von Ruette, J.; Lehmann, P.; Or, D. Effects of rainfall spatial variability and intermittency on shallow landslide triggering patterns at a catchment scale. *Water Resour. Res.* **2014**, *50*, 7780–7799. [CrossRef]
6. Torres, R.; Dietrich, W.E.; Montgomery, D.R.; Anderson, S.P.; Loague, K. Unsaturated zone processes and the hydrologic response of a steep, unchanneled catchment. *Water Resour. Res.* **1998**, *34*, 1865–1879. [CrossRef]
7. Johnson, K.A.; Sitar, N. Hydrologic conditions leading to debris-flow initiation. *Can. Geotech. J.* **1990**, *27*, 789–801. [CrossRef]
8. Hidayat, R.; Sutanto, S.J.; Hidayah, A.; Ridwan, B.; Mulyana, A. Development of a Landslide Early Warning System in Indonesia. *Geosciences* **2019**, *9*, 451. [CrossRef]
9. Chigira, M.; Kiho, K. Deep-seated rockslide-avalanches preceded by mass rock creep of sedimentary rocks in the Akaishi Mountains, central Japan. *Eng. Geol.* **1994**, *38*, 221–230. [CrossRef]
10. Chigira, M. September 2005 rain-induced catastrophic rockslides on slopes affected by deep-seated gravitational deformations, Kyushu, southern Japan. *Eng. Geol.* **2009**, *108*. [CrossRef]
11. Geertsema, M.; Clague, J.J.; Schwab, J.W.; Evans, S.G. An overview of recent large catastrophic landslides in northern British Columbia, Canada. *Eng. Geol.* **2006**, *83*, 120–143. [CrossRef]
12. Agliardi, F.; Crosta, G.B.; Frattini, P. Slow rock-slope deformation. In *Landslides*; Clague, J.J., Stead, D., Eds.; Cambridge University Press: Cambridge, UK, 2013; pp. 207–221.
13. Hungr, O.; Leroueil, S.; Picarelli, L. The Varnes classification of landslide types, an update. *Landslides* **2014**, *11*, 167–194. [CrossRef]
14. Hutchinson, J.N. General report: Morphological and geotechnical parameters of landslides in relation to geology and hydrogeology. *Int. J. Rock Mech. Min. Sci. Geomech. Abstr.* **1989**, *26*, 88. [CrossRef]
15. Bisci, C.; Burattini, F.; Dramis, F.; Leoperdi, S.; Pontoni, F.; Pontoni, F. The Sant'Agata Feltria landslide (Marche Region, central Italy): A case of recurrent earthflow evolving from a deep-seated gravitational slope deformation. *Geomorphology* **1996**, *15*, 351–361. [CrossRef]
16. Tsou, C.-Y.; Feng, Z.-Y.; Chigira, M. Catastrophic landslide induced by Typhoon Morakot, Shiaolin, Taiwan. *Geomorphology* **2011**, *127*, 166–178. [CrossRef]
17. Zerathe, S.; Lebourg, T. Evolution stages of large deep-seated landslides at the front of a subalpine meridional chain (Maritime-Alps, France). *Geomorphology* **2012**, *138*, 390–403. [CrossRef]
18. Petley, D.N.; Allison, R.J. The mechanics of deep-seated landslides. *Earth Surf. Process. Landf.* **1997**, *22*, 747–758. [CrossRef]

19. Ambrosi, C.; Crosta, G.B. Large sackung along major tectonic features in the Central Italian Alps. *Eng. Geol.* **2006**, *83*, 183–200. [CrossRef]
20. Miller, D.J.; Dunne, T. Topographic perturbations of regional stresses and consequent bedrock fracturing. *J. Geophys. Res. Solid Earth* **1996**, *101*, 25523–25536. [CrossRef]
21. Ambrosi, C.; Crosta, G.B. Valley shape influence on deformation mechanisms of rock slopes. *Geol. Soc. Lond. Spec. Publ.* **2011**, *351*, 215–233. [CrossRef]
22. Moro, M.; Saroli, M.; Salvi, S.; Stramondo, S.; Doumaz, F. The relationship between seismic deformation and deep-seated gravitational movements during the 1997 Umbria–Marche (Central Italy) earthquakes. *Geomorphology* **2007**, *89*, 297–307. [CrossRef]
23. Crosta, G. Landslide, spreading, deep seated gravitational deformation: Analysis, examples, problems and proposals. *Geogr. Fis. E Din. Quat.* **1997**, *19*, 297–313.
24. Barla, G. Numerical modeling of deep-seated landslides interacting with man-made structures. *J. Rock Mech. Geotech. Eng.* **2018**, *10*, 1020–1036. [CrossRef]
25. Padilla, C.; Onda, Y.; Iida, T.; Takahashi, S.; Uchida, T. Characterization of the groundwater response to rainfall on a hillslope with fractured bedrock by creep deformation and its implication for the generation of deep-seated landslides on Mt. Wanitsuka, Kyushu Island. *Geomorphology* **2014**, *204*, 444–458. [CrossRef]
26. Lv, H.; Ling, C.; Hu, B.X.; Ran, J.; Zheng, Y.; Xu, Q.; Tong, J. Characterizing groundwater flow in a translational rock landslide of southwestern China. *Bull. Eng. Geol. Environ.* **2019**, *78*, 1989–2007. [CrossRef]
27. Uchida, T.; Asano, Y.; Ohte, N.; Mizuyama, T. Seepage area and rate of bedrock groundwater discharge at a granitic unchanneled hillslope. *Water Resour. Res.* **2003**, *39*. [CrossRef]
28. Jitousono, T.; Shimokawa, E.; Teramoto, Y. Debris flow induced by deep-seated landslides at Minamata City, kumamoto prefecture, Japan in 2003. *Int. J. Eros. Control Eng.* **2008**, *1*, 5–10. [CrossRef]
29. Ebel, B.A.; Loague, K.; Montgomery, D.R.; Dietrich, W.E. Physics-based continuous simulation of long-term near-surface hydrologic response for the Coos Bay experimental catchment. *Water Resour. Res.* **2008**, *44*. [CrossRef]
30. Crozier, M.J. Prediction of rainfall-triggered landslides: A test of the Antecedent Water Status Model. *Earth Surf. Process. Landf.* **1999**, *24*, 825–833. [CrossRef]
31. Rahimi, A.; Rahardjo, H.; Leong, E.-C. Effect of antecedent rainfall patterns on rainfall-induced slope failure. *J. Geotech. Geoenviron. Eng.* **2011**, *137*, 483–491. [CrossRef]
32. Marino, P.; Peres, D.J.; Cancelliere, A.; Greco, R.; Bogaard, T.A. Soil moisture information can improve shallow landslide forecasting using the hydrometeorological threshold approach. *Landslides* **2020**, *17*, 2041–2054. [CrossRef]
33. Revellino, P.; Guadagno, F.M.; Hungr, O. Morphological methods and dynamic modelling in landslide hazard assessment of the Campania Apennine carbonate slope. *Landslides* **2008**, *5*, 59–70. [CrossRef]
34. De Vita, P.; Agrello, D.; Ambrosino, F. Landslide susceptibility assessment in ash-fall pyroclastic deposits surrounding Mount Somma-Vesuvius: Application of geophysical surveys for soil thickness mapping. *J. Appl. Geophys.* **2006**, *59*, 126–139. [CrossRef]
35. De Vita, P.; Napolitano, E.; Godt, J.W.; Baum, R.L. Deterministic estimation of hydrological thresholds for shallow landslide initiation and slope stability models: Case study from the Somma-Vesuvius area of southern Italy. *Landslides* **2013**, *10*, 713–728. [CrossRef]
36. Del Soldato, M.; Segoni, S.; De Vita, P.; Pazzi, V.; Tofani, V.; Moretti, S. Thickness model of pyroclastic soils along mountain slopes of Campania (southern Italy). In *Landslides and Engineered Slopes. Experience, Theory and Practice*; CRC Press: Boca Raton, FL, USA, 2016; pp. 797–804. ISBN 9781138029880.
37. Damiano, E.; Olivares, L. The role of infiltration processes in steep slope stability of pyroclastic granular soils: Laboratory and numerical investigation. *Nat. Hazards* **2010**, *52*, 329–350. [CrossRef]
38. Guadagno, F.M.; Forte, R.; Revellino, P.; Fiorillo, F.; Focareta, M. Some aspects of the initiation of debris avalanches in the Campania Region: The role of morphological slope discontinuities and the development of failure. *Geomorphology* **2005**, *66*, 237–254. [CrossRef]
39. Allocca, V.; Manna, F.; De Vita, P. Estimating annual groundwater recharge coefficient for karst aquifers of the southern Apennines (Italy). *Hydrol. Earth Syst. Sci.* **2014**, *18*, 803–817. [CrossRef]
40. Perrin, J.; Jeannin, P.-Y.; Zwahlen, F. Epikarst storage in a karst aquifer: A conceptual model based on isotopic data, Milandre test site, Switzerland. *J. Hydrol.* **2003**, *279*, 106–124. [CrossRef]

41. Hartmann, A.; Goldscheider, N.; Wagener, T.; Lange, J.; Weiler, M. Karst water resources in a changing world: Review of hydrological modeling approaches. *Rev. Geophys.* **2014**, *52*, 218–242. [CrossRef]
42. Petrella, E.; Capuano, P.; Carcione, M.; Celico, F. A high-altitude temporary spring in a compartmentalized carbonate aquifer: The role of low-permeability faults and karst conduits. *Hydrol. Process.* **2009**, *23*, 3354–3364. [CrossRef]
43. Bakalowicz, M. Epikarst. In *Encyclopedia of Caves*; Elsevier: Amsterdam, The Netherlands, 2012; pp. 284–288.
44. Di Maio, R.; De Paola, C.; Forte, G.; Piegari, E.; Pirone, M.; Santo, A.; Urciuoli, G. An integrated geological, geotechnical and geophysical approach to identify predisposing factors for flowslide occurrence. *Eng. Geol.* **2020**, *267*, 105473. [CrossRef]
45. Celico, F.; Naclerio, G.; Bucci, A.; Nerone, V.; Capuano, P.; Carcione, M.; Allocca, V.; Celico, P. Influence of pyroclastic soil on epikarst formation: A test study in southern Italy. *Terra Nov.* **2010**, *22*, 110–115. [CrossRef]
46. Cascini, L.; Sorbino, G.; Cuomo, S.; Ferlisi, S. Seasonal effects of rainfall on the shallow pyroclastic deposits of the Campania region (southern Italy). *Landslides* **2014**, *11*, 779–792. [CrossRef]
47. Comegna, L.; Damiano, E.; Greco, R.; Guida, A.; Olivares, L.; Picarelli, L. Field hydrological monitoring of a sloping shallow pyroclastic deposit. *Can. Geotech. J.* **2016**, *53*, 1125–1137. [CrossRef]
48. Greco, R.; Marino, P.; Santonastaso, G.F.; Damiano, E. Interaction between perched epikarst aquifer and unsaturated soil cover in the initiation of shallow landslides in pyroclastic soils. *Water* **2018**, *10*, 948. [CrossRef]
49. Marino, P.; Santonastaso, G.F.; Fan, X.; Greco, R. Prediction of shallow landslides in pyroclastic-covered slopes by coupled modeling of unsaturated and saturated groundwater flow. *Landslides* **2020**. [CrossRef]
50. Fusco, F.; De Vita, P.; Mirus, B.B.; Baum, R.L.; Allocca, V.; Tufano, R.; Di Clemente, E.; Calcaterra, D. Physically based estimation of rainfall thresholds triggering shallow landslides in volcanic slopes of southern Italy. *Water* **2019**, *11*, 1915. [CrossRef]
51. Trandafir, A.C.; Sidle, R.C.; Gomi, T.; Kamai, T. Monitored and simulated variations in matric suction during rainfall in a residual soil slope. *Environ. Geol.* **2008**, *55*, 951–961. [CrossRef]
52. Tsaparas, I.; Rahardjo, H.; Toll, D.G.; Leong, E.-C. Infiltration characteristics of two instrumented residual soil slopes. *Can. Geotech. J.* **2003**, *40*, 1012–1032. [CrossRef]
53. Hawke, R.; McConchie, J. In situ measurement of soil moisture and pore-water pressures in an 'incipient' landslide: Lake Tutira, New Zealand. *J. Environ. Manag.* **2011**, *92*, 266–274. [CrossRef]
54. Damiano, E.; Olivares, L.; Picarelli, L. Steep-slope monitoring in unsaturated pyroclastic soils. *Eng. Geol.* **2012**, *137–138*, 1–12. [CrossRef]
55. Papa, R.; Urciuoli, G.; Evangelista, A.; Nicotera, M. Field investigation on triggering mechanisms of fast landslides in unsaturated pyroclastic soils. In *Unsaturated Soils. Advances in Geo-Engineering*; Taylor & Francis: Abingdon, UK, 2008; pp. 909–915. ISBN 0415476925.
56. Pirone, M.; Papa, R.; Nicotera, M. Test site experience on mechanisms triggering mudflows in unsaturated pyroclastic soils in southern Italy. In *Unsaturated Soils*; CRC Press: Boca Raton, FL, USA, 2010; pp. 1273–1278. ISBN 9780415604307.
57. Kosugi, K.; Katsura, S.; Katsuyama, M.; Mizuyama, T. Water flow processes in weathered granitic bedrock and their effects on runoff generation in a small headwater catchment. *Water Resour. Res.* **2006**, *42*. [CrossRef]
58. Salve, R.; Rempe, D.M.; Dietrich, W.E. Rain, rock moisture dynamics, and the rapid response of perched groundwater in weathered, fractured argillite underlying a steep hillslope. *Water Resour. Res.* **2012**, *48*. [CrossRef]
59. Brönnimann, C.; Stähli, M.; Schneider, P.; Seward, L.; Springman, S.M. Bedrock exfiltration as a triggering mechanism for shallow landslides. *Water Resour. Res.* **2013**, *49*, 5155–5167. [CrossRef]
60. Fiorillo, F.; Guadagno, F.; Aquino, S.; De Blasio, A. The December 1999 Cervinara landslides: Further debris flows in the pyroclastic deposits of Campania (southern Italy). *Bull. Eng. Geol. Environ.* **2001**, *60*, 171–184. [CrossRef]
61. Comegna, L.; Damiano, E.; Greco, R.; Guida, A.; Olivares, L.; Picarelli, L. Effects of the vegetation on the hydrological behavior of a loose pyroclastic deposit. *Procedia Environ. Sci.* **2013**, *19*, 922–931. [CrossRef]
62. Greco, R.; Comegna, L.; Damiano, E.; Guida, A.; Olivares, L.; Picarelli, L. Hydrological modelling of a slope covered with shallow pyroclastic deposits from field monitoring data. *Hydrol. Earth Syst. Sci.* **2013**, *17*, 4001–4013. [CrossRef]
63. Rolandi, G.; Bellucci, F.; Heizler, M.T.; Belkin, H.E.; De Vivo, B. Tectonic controls on the genesis of ignimbrites from the Campanian Volcanic Zone, southern Italy. *Mineral. Petrol.* **2003**, *79*, 3–31. [CrossRef]

64. Greco, R.; Guida, A. Field measurements of topsoil moisture profiles by vertical TDR probes. *J. Hydrol.* **2008**, *348*, 442–451. [CrossRef]
65. Topp, G.C.; Davis, J.L.; Annan, A.P. Electromagnetic determination of soil water content: Measurements in coaxial transmission lines. *Water Resour. Res.* **1980**, *16*, 574–582. [CrossRef]
66. Capparelli, G.; Spolverino, G.; Greco, R. Experimental Determination of TDR Calibration Relationship for Pyroclastic Ashes of Campania (Italy). *Sensors* **2018**, *18*, 3727. [CrossRef]
67. Greco, R.; Guida, A.; Damiano, E.; Olivares, L. Soil water content and suction monitoring in model slopes for shallow flowslides early warning applications. *Phys. Chem. Earth Parts A/B/C* **2010**, *35*, 127–136. [CrossRef]
68. McDonnell, J.J.; Stewart, M.K.; Owens, I.F. Effect of catchment-scale subsurface mixing on stream isotopic response. *Water Resour. Res.* **1991**, *27*, 3065–3073. [CrossRef]
69. Pellerin, B.A.; Wollheim, W.M.; Feng, X.; Vörösmarty, C.J. The application of electrical conductivity as a tracer for hydrograph separation in urban catchments. *Hydrol. Process.* **2008**, *22*, 1810–1818. [CrossRef]
70. Pearce, A.J.; Stewart, M.K.; Sklash, M.G. Storm runoff generation in humid headwater catchments: 1. Where does the water come from? *Water Resour. Res.* **1986**, *22*, 1263–1272. [CrossRef]
71. Hargreaves, G.H.; Allen, R.G. History and evaluation of hargreaves evapotranspiration equation. *J. Irrig. Drain. Eng.* **2003**, *129*, 53–63. [CrossRef]
72. Blaney, H.F.; Criddle, W.D. *Determining Consumptive Use and Irrigation Water Requirements*; US Department of Agriculture: Washington, DC, USA, 1962.
73. Doorenbos, J.; Pruitt, W.O. *Crop Water Requirements*; FAO Irrigation and Drainage Paper 24; FAO: Rome, Italy, 1977; ISBN 9251002797.
74. Monteith, J.L. Evaporation and environment. In *Symposia of the Society for Experimental Biology*; Cambridge University Press: Cambridge, UK, 1965.
75. Thornthwaite, C.W. An Approach toward a Rational Classification of Climate. *Geogr. Rev.* **1948**, *38*, 55. [CrossRef]
76. Breuer, L.; Eckhardt, K.; Frede, H.-G. Plant parameter values for models in temperate climates. *Ecol. Modell.* **2003**, *169*, 237–293. [CrossRef]
77. Cutini, A.; Matteucci, G.; Mugnozza, G.S. Estimation of leaf area index with the Li-Cor LAI 2000 in deciduous forests. *For. Ecol. Manag.* **1998**, *105*, 55–65. [CrossRef]
78. Körner, C.; Ja, S. Maximum leaf diffusive conductance in vascular plants. *Photosynthetica* **1979**, *13*, 45–82.
79. Shuttleworth, W.J. Evaporation. In *Handbook of Hydrology*; Maidment, D.R., Ed.; McGraw-Hill: New York, NY, USA, 1993; ISBN 0070397325.
80. Testa, G.; Gresta, F.; Cosentino, S.L. Dry matter and qualitative characteristics of alfalfa as affected by harvest times and soil water content. *Eur. J. Agron.* **2011**, *34*, 144–152. [CrossRef]
81. Allen, R.G.; Pereira, L.S.; Smith, M.; Raes, D.; Wright, J.L. FAO-56 dual crop coefficient method for estimating evaporation from soil and application extensions. *J. Irrig. Drain. Eng.* **2005**, *131*, 2–13. [CrossRef]
82. Pirone, M.; Papa, R.; Nicotera, M.V.; Urciuoli, G. Evaluation of the hydraulic hysteresis of unsaturated pyroclastic soils by in situ measurements. *Procedia Earth Planet. Sci.* **2014**, *9*, 163–170. [CrossRef]
83. De Vita, P.; Fusco, F.; Tufano, R.; Cusano, D. Seasonal and event-based hydrological and slope stability modeling of pyroclastic fall deposits covering slopes in Campania (Southern Italy). *Water* **2018**, *10*, 1140. [CrossRef]